

Seasonal forecast of tropical cyclones in the Southwest Pacific Ocean

Sara O. van Vloten¹  | Andrea Pozo^{2,3} | Laura Cagigal¹ | Fernando J. Méndez¹

¹Geomatics and Ocean Engineering Group, Departamento de Ciencias y Técnicas del Agua y del Medio Ambiente, ETSICCP, Universidad de Cantabria, Santander, Spain

²Geospatial Research Institute, University of Canterbury, Christchurch, New Zealand

³School of Earth and Environment, University of Canterbury, Christchurch, New Zealand

Correspondence

Laura Cagigal, Geomatics and Ocean Engineering Group, Departamento de Ciencias y Técnicas del Agua y del Medio Ambiente, ETSICCP, Universidad de Cantabria, Santander, Spain.
Email: laura.cagigal@unican.es

Funding information

Spanish Ministry of Science and Innovation; Juan de la Cierva-Formación FJC2021-046933-I/MCIN/AEI/10.13039/501100011033; European Union "NextGenerationEU"/PRTR

Abstract

Predictions of tropical cyclone (TC) activity have been a topic of recurrent interest and research in the past. Here we utilize reanalysis datasets of sea surface temperature (SST) and mixed layer depth (MLD) to build a statistical seasonal forecasting model that produces outlooks of expected TC counts in the region of the Southwest Pacific (SWP). Nevertheless, the model applicability can be extended to other regions and basins. A novel TC predictor index is developed at the daily scale and used to obtain an objective classification of synoptic weather patterns. This classification has been performed by clustering the daily index predictor fields, previously transformed into principal components, using a *K*-mean algorithm. As a result, 49 daily weather types (DWTs) are presented which inform about the mean representative features and spatial patterns of both predictor and predictand variables. Thus, statistical relationships between TC activity and nonlinear combinations of predictor variables are found to assign daily rates of expected TCs. The cluster-based model is calibrated from 1982 to 2019 and validated by recent TC season observations, demonstrating the operational application using ensembles of long-term predictions in the Southwest Pacific. Results have shown which synoptic types of SST and MLD are favourable to cyclogenesis and activity, with additional information related to concurrent sea level pressure and precipitation synoptic patterns, as well as seasonal and interannual climate variability.

KEYWORDS

daily weather types, mixed layer depth, sea surface temperature, seasonal forecast, tropical cyclones

1 | INTRODUCTION

Tropical cyclones (TCs) that form over warm tropical oceans are one of the most destructive weather phenomena, with a high potential to damage coastal installations due to their extreme winds, heavy rainfall, flooding and

storm surges (Emanuel, 2003). The risk level is particularly elevated for highly populated low-lying island nations due to their inherent vulnerability and limited capacity to build resilience under such adverse conditions. Thus, damage induced by the passage of TCs is a major concern in many tropical Pacific islands, which

This is an open access article under the terms of the [Creative Commons Attribution-NonCommercial-NoDerivs](https://creativecommons.org/licenses/by-nc-nd/4.0/) License, which permits use and distribution in any medium, provided the original work is properly cited, the use is non-commercial and no modifications or adaptations are made.

© 2023 The Authors. *International Journal of Climatology* published by John Wiley & Sons Ltd on behalf of Royal Meteorological Society.

makes it valuable to build long-term prediction tools in addition to short-term early warning systems. However, the task of producing seasonal forecasts of TC activity requires an understanding of historical TC seasons in order to identify key drivers such as environmental conditions, their interrelationships and teleconnections. This may significantly contribute to estimating accurate upcoming season outlooks, and to improve the population preparedness and capacity to manage upcoming adverse impact in advance of each TC season. Generally, the North Atlantic and Northwest Pacific oceans have received more attention with a greater number of studies compared to the Southwest Pacific (SWP), since the former regions exhibit the most active tropical cyclogenesis and these oceans are bound by increasingly populated long coastlines likely to be hit by TCs. However, the SWP hosts many small islands developing states (SIDS) with limited resources, a growing population and a large susceptibility to natural disasters. These island countries are especially vulnerable and often struck or severely affected by the passage of TCs. During the last two TC seasons, two category 5 events struck this region, in addition to a total number of cyclones similar to the average during the last four decades. In the late 2019–2020 season, TC Harold (April 2020) caused destruction in Solomon Islands, Vanuatu, Fiji and Tonga, and in the following early 2020–2021 season, TC Yasa (December 2020) also affected Vanuatu, Fiji and Tonga with estimated damages of 250 M USD to infrastructure, livelihoods and agriculture (Refugees International, 2022).

Past research studies established positive and negative trends between various environmental variables and TC activity which are also subjected to various local and global climate dynamics and teleconnections (e.g., Basher & Zheng, 1995; Diamond et al., 2013; Nicholls, 1979; Patricola et al., 2016). Tropical cyclones are rotating low-pressure weather systems with very intense winds forming over tropical oceans (Smith, 2006). Furthermore, it is well-known that the ocean surface temperature and heat content are necessary conditions for genesis, intensification and development of TCs (Dowdy et al., 2012); this is consistent with tropical latitudes (5° – 20° S) generally experiencing warmer sea surface temperatures (SST). Additionally, a number of large-scale environmental variables are closely connected with climatological features of the seasonal frequency of TC genesis; one key parameter that promotes the development and intensification of TCs is weak-to-moderate vertical wind shear (Gray, 1979); negative (vertical) vorticity in the Southern Hemisphere is more favourable for cyclogenesis (Camargo et al., 2007); high values of relative humidity are required during the development stage as it allows deep moist convection and the formation of thunderstorm cloud bands (Pillay & Fitchett, 2021). Out of these factors,

generally the SST has been used to predict TC activity and intensification since it is a very representative factor of the available thermal ocean energy. The El Niño–Southern Oscillation (ENSO) climate pattern has appeared to strongly influence the location of TC genesis (e.g., Chand & Walsh, 2009), since different ENSO phases control changes of SST longitudinal gradients. Moreover, the ocean mixed layer depth (MLD) is a secondary indicator for higher upper ocean heat content that mainly influences storm intensity (e.g., Vissa et al., 2012).

A number of studies have contributed to the prediction of seasonal activity of TCs. Particularly, statistical models explore relationships between large-scale drivers influencing TC occurrence, frequency, intensity and preferred tracks in some regions (Pielke & Landsea, 1999). In the SWP region, different approaches have been developed; the NIWA's (National Institute of Water and Atmospheric research) Pacific outlook provides the expected TC activity and TC risk based on the selection of analogue past seasons that describe the climate state (Coupled ENSO Index [CEI]; Gergis & Fowler, 2005) leading into the upcoming TC season; the Australian Bureau of Meteorology (BOM) outlook uses the statistical relationships between TC activity and two indicators that provide a measure of the atmospheric (the Southern Oscillation Index [SOI]) and oceanic (the Niño3.4 SST anomaly) state of the ENSO; the long-range Tropical Cyclone Outlook for the SWP (TCO-SP) is a deterministic (frequency) and probabilistic (likelihood) statistical model calibrated using IBTrACS and several key climate indices (NINO1+2, NINO3, NINO3.4, NINO4, SOI, CEI, Oceanic Niño Index [ONI], Trans Niño Index [TNI], ENSO Modoki Index [EMI], ENSO Longitude Index [ELI]) representing interannual Indo-Pacific climate variability for the Southern Hemisphere (Magee et al., 2020); the Fiji Meteorological Service (FMS) outlook is based upon analogue status of the ENSO over the May–September period leading to the TC season.

While the use of various climate indices as predictors has been explored in the past, here we propose a cluster-based statistical model using data mining techniques to obtain an objective classification of spatial fields of a novel TC index in the SWP built over spatial fields of the SST and MLD. This model is trained with reanalysis datasets to establish the predictor–predictand relationship. This relationship will then be used to obtain the probabilistic seasonal forecast based on the ensemble of operational global predictions of SST and MLD.

This paper is structured as follows: section 2 presents the study site and the various datasets used; section 3 describes the proposed methodology with the construction of the index predictor and the obtention of synoptic weather types; section 4 analyses the time-scales

variability that can be derived from the resulting classification; section 5 presents additional results extracted from atmospheric variables; section 6 presents the forecast model application and the model validation; and section 7 concludes with a summary and discussion.

2 | DATA AND STUDY SITE

This paper focuses on the SWP Ocean in a target region defined as the area between 0° and 30°S in latitude and between 160° and 210°E in longitude, covering from the eastern Solomon Islands to the western French Polynesia (Figure 1), thus focusing on Fiji, Samoa and Tonga and the surrounding areas. The whole study site is a wide area historically affected by TCs, and it includes the major generation area in the South Pacific basin. The historical record (IBTrACS-WMO) of TCs in the SWP indicates an average of 7.4 cyclones per season over 37 years (1981–2019) which is used as the calibration period in the present work, and the number of cyclones ranges from 3 to 15 per season, with a total of 275 TCs, of which 103 were severe storms (category 3 or higher, as defined later in section 3.2). Figure 1 illustrates the island territories and the season average number of historical observed TCs in the period 1981–2019. For the purpose of this study, the datasets presented in the following subsections were retrieved in the depicted regional influence area to build the proposed tailor-made index predictor, and to implement the model.

2.1 | Tropical cyclones

TC data were obtained from the International Best Track Archive for Climate Stewardship (IBTrACS) which is a centralized compilation of global available records and estimates of historical storm tracks from several observational sources (Knapp et al., 2010, 2018), namely the Regional Specialized Meteorological Centers (RSMCs), since 1851 onwards. Here no RMSC was selected in particular but instead the World Meteorological Organization (WMO), which provides the official data reported by the responsible agency at each location. The IBTrACS version 04r00 database includes the storm track position (longitude and latitude), the central pressure and the maximum wind speed at 6-h intervals. In this study we have used the track location and the associated central pressure, representative of the storm intensity because it is easily comparable between different agencies, contrary to some inhomogeneities of procedures used by RSMCs to report maximum sustained winds.

2.2 | Sea surface temperature

The NOAA high-resolution SST was developed using an optimum interpolation (OI) technique, combining observations from satellite data, ships, buoys on a global grid, and interpolating to fill in spatial gaps (Huang et al., 2020). The OISST has a spatial grid resolution of 0.25° and provides mean daily data available from

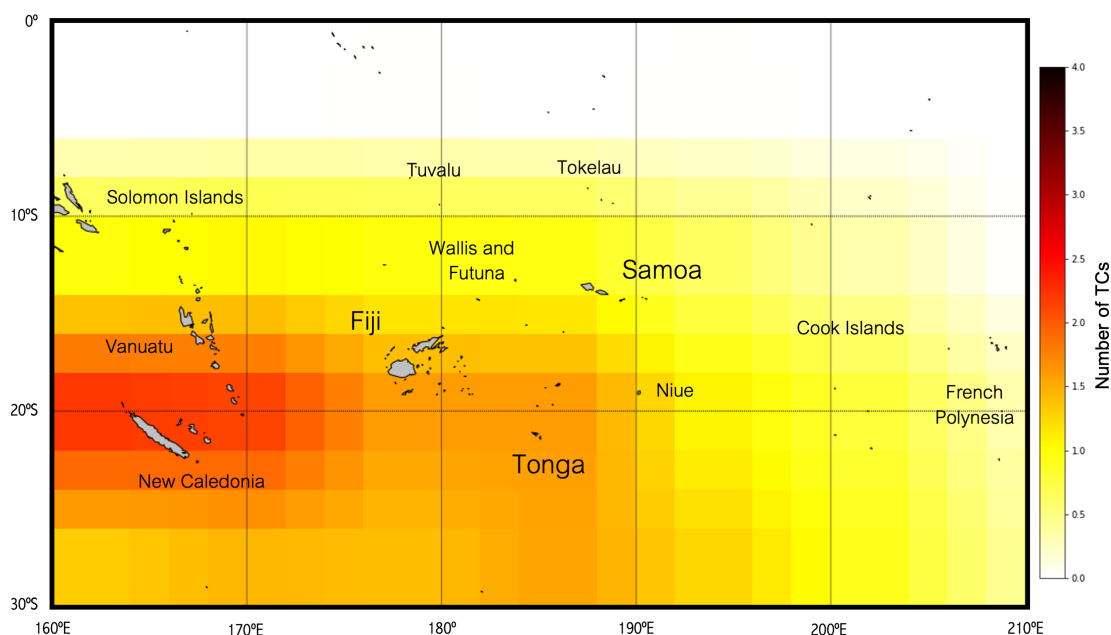


FIGURE 1 Map of the SWP tropical islands within the study area, from 160°E to 210°E and 0° to 30°S , and the season average number of TCs (1981–2019) [Colour figure can be viewed at wileyonlinelibrary.com]

September 1981 to the present. Therefore, we collected mean daily SST in the study domain for a period spanning 40 years.

2.3 | Mixed layer depth, mean sea level pressure

The Climate Forecast System Reanalysis (CFSR) was developed by the NOAA's National Centers for Environmental Prediction (NCEP), and it is a reanalysis product executed as a global, high-resolution, coupled atmosphere–ocean–land surface–sea ice system to provide the best estimate of the state of these coupled domains (Saha et al., 2010), spanning a period from January 1979 until March 2011. In addition, the CFS model was also extended as the CFSv2 Operational Analysis product (Saha et al., 2014) from April 2011 to present. Mean daily data of MLD and mean sea level pressure (MSLP) are available at a spatial resolution of 0.25° at the equator, extending to 0.5° beyond the Tropics.

2.4 | Precipitation

Mean daily precipitation data was extracted from the Tropical Rainfall Measuring Mission (TRMM, 2011) which was a research satellite in operation from 1997 to 2015, with the purpose of improving the understanding of spatial variability and distribution of precipitation within the Tropics. The TRMM Multi-satellite Precipitation Analysis (TMPA) algorithm provides the 3B42 dataset with precipitation estimates with a temporal coverage of 3 h, and a spatial resolution of 0.25°.

2.5 | Forecast data

To construct future daily fields of the index predictor, we use the CFSv2 operational forecast (<https://www.ncei.noaa.gov/access/metadata/landing-page/bin/iso?id=gov.noaa.ncdc:C00877>) to download and collect daily predictions of SST and MLD. The four-times-daily, 9-month control runs, consist of 6-hourly forecasts time-series. The period of record began on April 2011 and continues onwards; therefore, it is possible to validate the model and evaluate the skill of the methodology of past TC seasons, as well as to apply the model with ongoing forecasts.

2.6 | Climate indices

Two climate indices from the NOAA were used. On one hand, monthly time series of the Niño3.4 which is the

area averaged SST from 5°N to 5°S and 170°W to 120°W, calculated as the anomaly removing the 1981–2010 mean (https://psl.noaa.gov/gcos_wgsp/Timeseries/Nino34). On the other hand, the Tripole Index for the Interdecadal Pacific Oscillation (IPO), which is based on the difference between SSTA averaged over the central equatorial Pacific and the average of SSTA in the Northwest and Southwest Pacific (<https://psl.noaa.gov/data/timeseries/IPOTPI>).

3 | STATISTICAL MODEL

3.1 | Methodology overview

The proposed methodology aims to produce seasonal forecasts of TC activity in the SWP regional area defined in Figure 1, based on historical and statistical relationships between TC occurrence and the concurrent spatial configurations of two key oceanic drivers (SST and MLD). Since predictor datasets are available in a common timeframe from 1982 onwards, the model is calibrated for the period 1982–2019, while the skill of the model is assessed through the two most recent seasons 2020–2022 observations. Also, the model's performance is evaluated for the most recent years 2011–2022 based on past reforecasts. Figure 2 illustrates the flow chart of the proposed methodology. First, information of SST, MLD and historical storm tracks' central pressure is used to develop an index that informs of the combinations of SST and MLD that have the potential to produce TCs, and also on the intensity of the TCs produced based on past TCs in the study area. Then, the statistical model is built by means of the principal component analysis (PCA) dimension-reduction technique combined with a clustering algorithm to obtain an objective classification of synoptic patterns that represent the spatial variability of the index predictor at a daily scale. Next, the statistical relationship between the predictor patterns and the occurrence rates of TC activity is found. Once the statistical model is built and validated, it is implemented with operational forecasts of both SST and MLD. In the following subsections, each step of the methodology is further explained.

3.2 | Index predictor

In past studies, the SST variable has been considered the primary thermodynamical driver to trigger and sustain TC seasonal activity (Espejo et al., 2014). However, in this study a combined index is used instead to also account for the interplay of the SST and MLD during

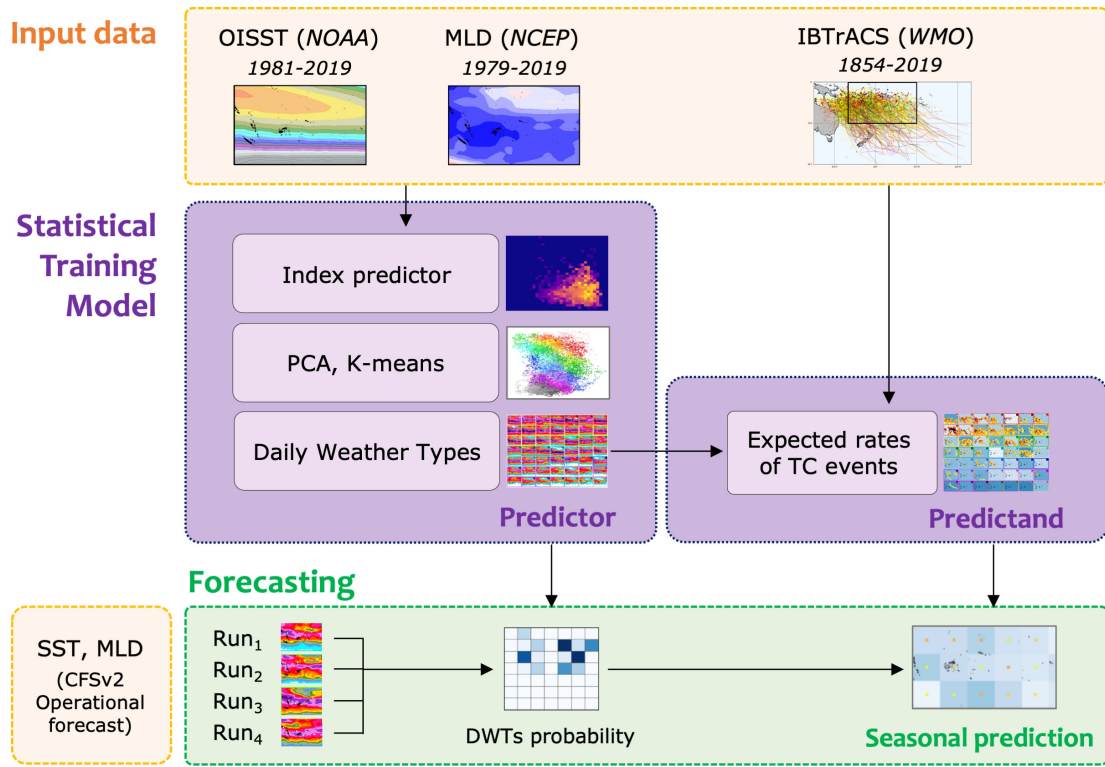


FIGURE 2 Flow chart of the methodology [Colour figure can be viewed at wileyonlinelibrary.com]

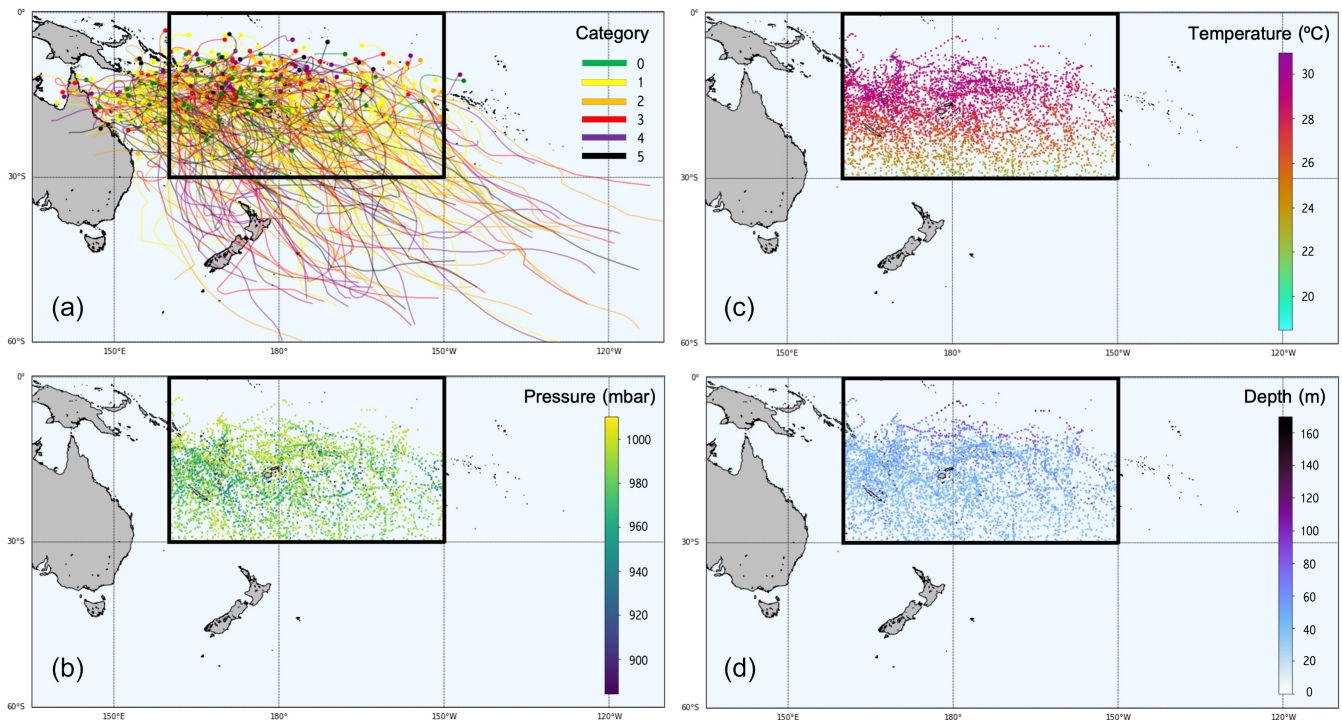


FIGURE 3 Maps of the SWP basin and datasets of (a) historical storm tracks from 1982 to 2019 (IBTrACS-WMO) that enter the study area (black rectangle), and the associated values at each storm location of (b) central pressure, (c) SST and (d) MLD [Colour figure can be viewed at wileyonlinelibrary.com]

cyclogenesis and throughout the lifetime of active storms. For that purpose, both datasets plus the historical TCs central pressure were extracted for the calibration timeframe spanning from 1982 to 2019. Figure 3 provides an overview of the spatial distribution of the collected data within the study area (black rectangle) in the SWP. Figure 3a depicts the tracks of historical TCs (IBTrACS-WMO) that either were generated in, entered or crossed the target area; the dots indicate the genesis location while the colour is representative of the maximum category reached by each TC. Here, categories are defined by central pressure ranges as follows: categories 5, 4, 3, 2, 1 correspond to central pressure values lower than 920, 944, 964, 979 and 1000 mbar, respectively, and category 0 accounts for values higher than 1000 mbar. It can be noticed that our target area encompasses a widespread extension which includes the majority of genesis positions while others originate in the Coral Sea, further to the west of Solomon Islands, and later such storms enter the study area as they move either eastwards or southeast. Figure 3b shows the coordinates of active storms coloured with the corresponding central pressure values ranging between 884 and 1010 mbar. Higher storm intensities generally occur in the belt latitudes 10°–20°S, and storm locations are more concentrated west to the international dateline, while east to Fiji storms are comparatively more scattered. Figure 3c,d

shows the associated values of SST and MLD, respectively, interpolated at each track position. SST values show a zonal stratification of temperatures ranging between 20 and 32°C, decaying more rapidly from latitudes near the Tropic of Capricorn towards the South Pole. In contrast, MLD values do not show a well-defined stratification pattern although low latitudes tend to present larger depths especially during the austral winter months.

The collected database with information of concurrent values of storm intensity, and the two oceanic variables can be visualized in a discretized 2D-plot (Figure 4), by aggregating surface temperatures every 0.5°C, and water depths every 5 m. Each resulting bin is assigned with the minimum value of central pressures that fall under each combination of SST and MLD, thereby considering the most intense observation that is likely to occur. Finally, the index predictor is defined as the standardized minimum central pressure between [0, 1]. Maximum index values, meaning the lowest central pressures or most intense TC categories, generally take place when the SST is warmer than 28°C and below 30°C, whereas the MLD is between 20 and 70 m depth. Similarly, other relations can be inferred from historical data in the regional study area; no TC activity is observed whenever SST is higher than 31°C or lower than 19°C; there are seldom storm observations when MLD is larger than 120 m; the joint probability distribution describes

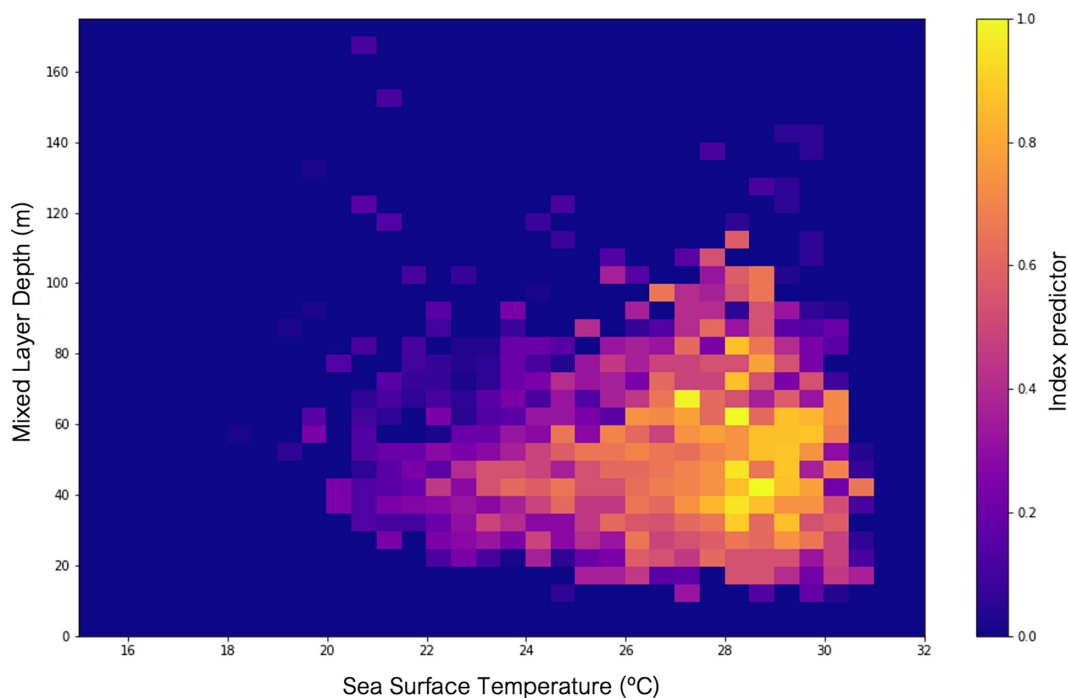


FIGURE 4 Index predictor built from standardized central pressures between 884 and 1004 mbar, with predictor variables discretized every 0.5°C (x-axis SST) and 5 m (y-axis MLD) [Colour figure can be viewed at wileyonlinelibrary.com]

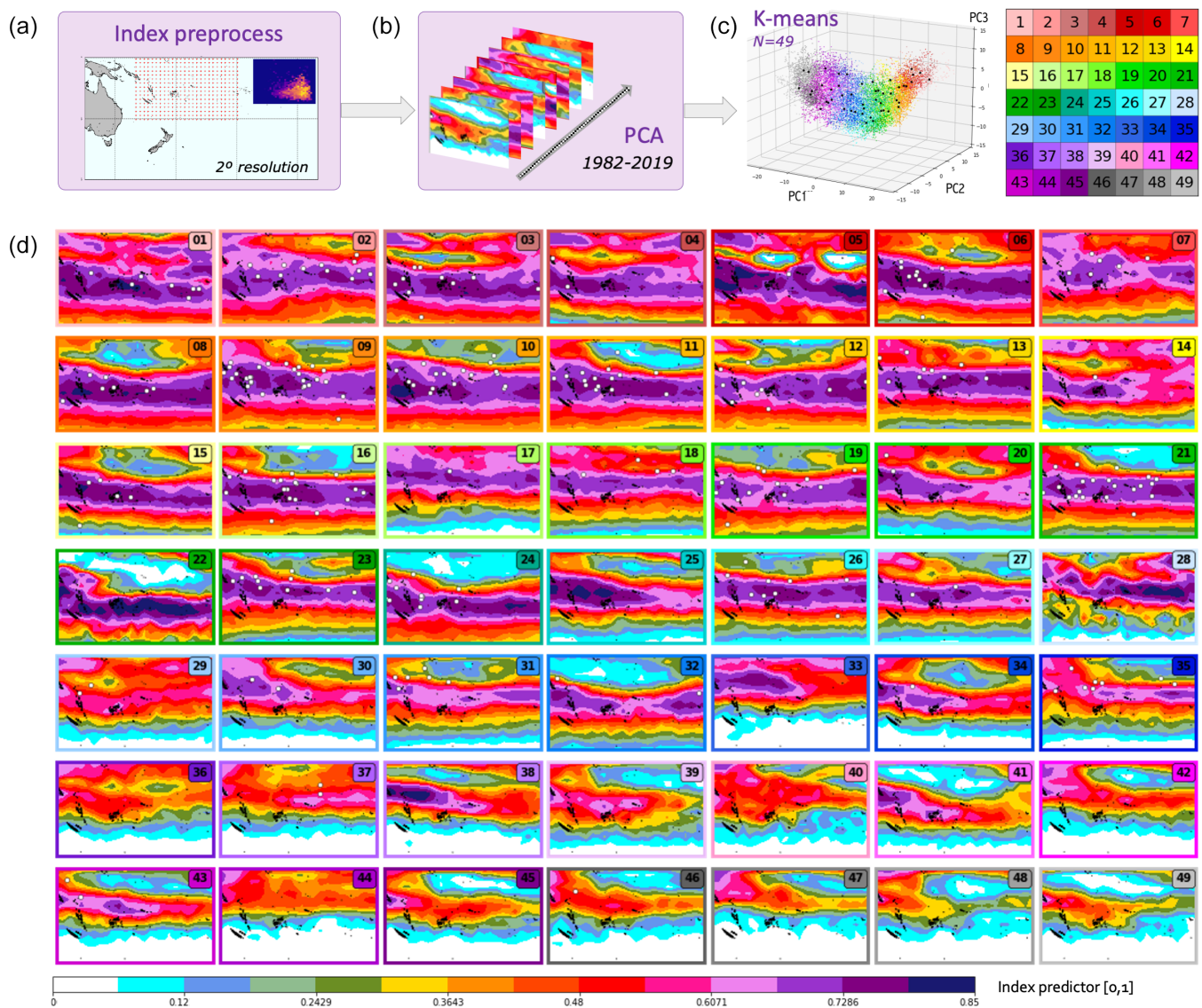


FIGURE 5 Methodology workflow: (a) index predictor daily fields using 2° grid resolution; (b) sketch representing the PCA over the series of index daily fields along the calibration period (1982–2019); (c) *K*-means of 49 clusters (black/coloured dots represent the 49 centroids and the whole dataset) represented as a function of the three first PCs and the colourmap code; and (d) classification of $M = 49$ DWTs of the index predictor displayed in a lattice with ordered spatial variations (white dots indicate TC genesis locations) [Colour figure can be viewed at [wileyonlinelibrary.com](https://onlinelibrary.wiley.com/doi/10.1002/joc.8295)]

that as SST lowers down so does MLD, especially for occurrences of severe storms.

3.3 | Statistical downscaling

The goal of the statistical downscaling is to identify mean synoptic spatial configurations of the index predictor in the SWP Ocean, and their corresponding expected rates of TC activity so that a probabilistic relationship can be established to be used in the seasonal forecast. In that context, the proposed tailor-made index facilitates the aggregation of SST and MLD at a daily scale in a 2° grid resolution over the study domain (Figure 5a) during

the calibration period. Next, the series of daily index maps from 1st January 1982 to 31st December 2019 is used to perform a PCA (Figure 5b) reducing the dimensionality of the original data and transforming the index fields into spatial and temporal modes. The calibration data is originally composed of $N \approx 38 \times 365 = 13,870$ daily fields of the index predictor, $\{\text{Index}(x, t_1), \text{Index}(x, t_2), \dots, \text{Index}(x, t_N)\}$, where x represents the geographic location and t represents the time in days. The original data can be explained as a linear combination of Eigen orthogonal functions (EOFs) and principal components (PCs): $\text{Index}(x, t) = \text{EOF}_1(x) \cdot \text{PC}_1(t) + \text{EOF}_2(x) \cdot \text{PC}_2(t) + \dots + \text{EOF}_{N_g}(x) \cdot \text{PC}_{N_g}(t)$, with N_g the dimension or number of data grid points. Moreover, the index spatial fields can

be approximated by taking only the first PCs that explain 90% of the variance ($n=237$), therefore preserving the dominant spatial variability patterns with their corresponding temporal amplitude coefficients while neglecting the remaining PCs which explain residual variance.

The next step deals with producing synoptic index patterns by applying a clustering K -means algorithm over the n principal components $\{PC_1(t), PC_2(t), \dots, PC_n(t)\}$ to obtain a reduced number of M clusters, so that each daily index field may be grouped with other similar spatial configurations. Therefore, each cluster can be represented by a centroid or prototype so that for the k th cluster we have $\text{Index}_k = \{PC_{1,k}, PC_{2,k}, \dots, PC_{n,k}\}$ with $k=1, \dots, M$. Furthermore, it is possible to express those centroids in the original data space with the corresponding spatial modes to each PC as $\text{Index}_k(x) = \{EOF_1(x)PC_{1,k} + EOF_2(x)PC_{2,k} + \dots + EOF_n(x)PC_{n,k}\}$ with $k=1, \dots, M$. Several K -means tests were performed with different number of clusters and eventually, we chose a classification of $M=49$ daily weather types (DWTs). The criteria followed to determine the number of M groups was to ensure that: (a) there was a sufficient amount of different and representative spatial patterns to characterize the whole spatial variability of the data, (b) the mean number of members per group is close to $N/M=13,870/49 \approx 280$, (c) the minimum number of members per group is 50, and (d) the members belonging to the same cluster are well represented by its centroid, meaning that the group members are homogeneous among them.

Figure 5c illustrates the resulting K -means clustering of 49 DWTs in the space of the first three PCs, with small dots representing daily index fields which are coloured according to the cluster they belong to, following a sequential colourmap code of 49 colours. Therefore, minimum Euclidean distances were calculated from every daily index field to the M centroids in order to assign the nearest (and most similar) k -cluster, namely the best match unit. Figure 5d shows the resulting classification of 49 DWTs, displayed in a lattice with ordered spatial variations to facilitate visual analysis, along with coloured box frames matching the aforementioned colour code (Figure 5c). Spatial maps are coloured with the index predictor indicating its intensity from low to high in a scale from 0 to 0.85. Moreover, white dots represent the location of historical TCs genesis in each corresponding DWT. A more or less consistent high intensity belt (index > 0.6) can be observed in latitudes around 15°S in the first 28 DWTs, with a variety of the belt thicknesses and strengths. The remaining patterns in the lower part of the lattice show smaller index values. Cyclogenesis are generally located over such belts with some exceptions, and some

DWTs tend to concentrate more genesis events, either evenly spread over the belt (DWTs 2, 9, 10, 16, 19, 21, 23) or more intensively gathered on the left side of the domain (DWTs 3, 6, 11, 12, 24, 26, 31), generally to the west of Samoa. In particular, it can be noticed that DWT 5, 22, 25, 28, 38 have not registered genesis events although their index reaches maximum values up to 0.85. Also, genesis seldom occurs whenever the index is below 0.1 (white–cyan) starting from 15°S to 20°S latitudes poleward.

Furthermore, it is possible to gain some understanding on the physical contributions behind the index by plotting the associated mean synoptic conditions of SST and MLD (Figure 6a shows temperature maps and depth contour lines). It can be seen that geneses are more likely triggered by warm surface temperatures (especially near the 29°C isotherm) together with contour depths between 50 and 75 m (depending on the season), which is consistent with the index predictor definition presented in section 3.1. Regarding the surface temperature configurations, some patterns depict a warmer area under the equator and north to Fiji (DWTs 19, 22, 25, 26, 28, 32, 41); and the shape of isotherms can be either zonal or bending to the south, and of various size areas. Generally, a common feature of cyclogenesis is that their locations generally occur either south or north of the warmest SST area, rather than within such area. Regarding the MLD configurations, the upper part of the lattice exhibits zonal or southeast 50 m contour depths around 20°S latitudes, while the lower lattice is characterized by a more chaotic spatial distribution as well as more pronounced depths. These two trends typically correspond to austral summer and winter months, respectively, when stronger storm winds tend to deepen MLD (Zhang et al., 2018).

The next step to train the statistical model consists of defining the predictand, thus establishing the statistical relationship between the index predictor DWTs and their associated expected TC rates of occurrence. For that purpose, the domain is divided into subareas of $8^\circ \times 8^\circ$, building in each of them a counter of days for whenever a track enters the region, thus evaluating all historical TCs and computing the number of active days in each DWT, $\text{Counter} = \{C_{j,\text{DWT}_1}, C_{j,\text{DWT}_2}, \dots, C_{j,\text{DWT}_{49}}\}$, with $j=1, \dots, S$ the number of subareas, in this case $S=28$. The resulting predictand is the ratio of expected number of TCs conditioned by the occurrence of a certain DWT, which is calculated as the daily track counter divided by the total number of days of the corresponding DWT, as $\text{Ratio} = \left\{ \frac{C_{j,\text{DWT}_1}}{N_{\text{DWT}_1}}, \frac{C_{j,\text{DWT}_2}}{N_{\text{DWT}_2}}, \dots, \frac{C_{j,\text{DWT}_{49}}}{N_{\text{DWT}_{49}}} \right\}$, with $j=1, \dots, S$. Figure 6b shows the outcome with coloured cells indicating storm activity, with darker colours depicting highest rates of TC activity, which are mostly concentrated in the upper part

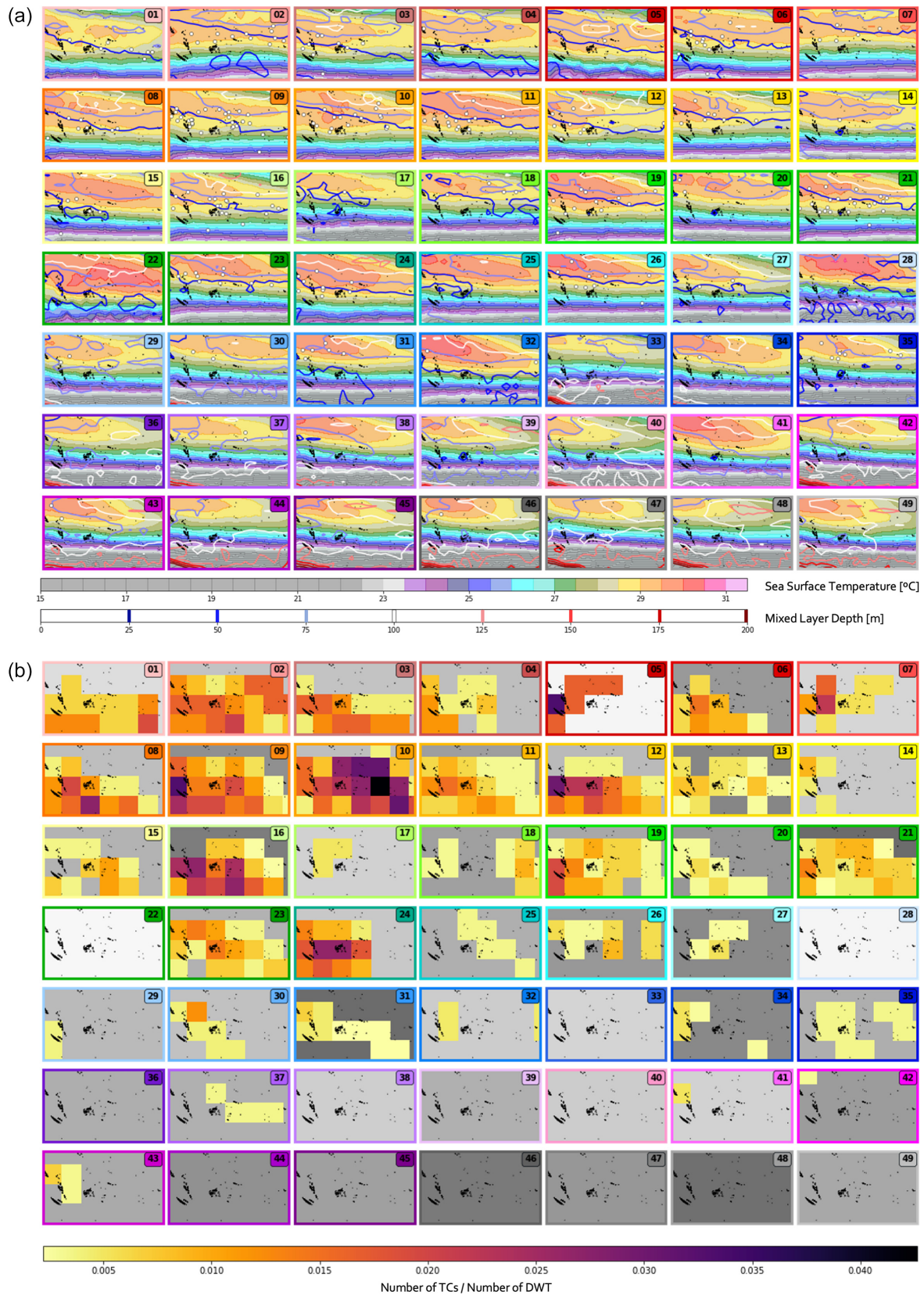


FIGURE 6 Classification of $M = 49$ DWTs of (a) predictor variables SST (colourmaps ranging from 15 to 31°C) and MLD (contour lines ranging from 0 to 200 m depth) with white dots indicating TC genesis locations; and of (b) predictand of daily expected TC rates of occurrence conditioned by each DWT in 8° squared subareas (background gradation colour indicates the marginal DWT probabilities as in Figure 7a) [Colour figure can be viewed at wileyonlinelibrary.com]

of the DWT lattice. The grey background colour indicates the marginal occurrence probability of each DWT with DWTs 6, 9, 13, 16, 21 showing higher occurrence.

4 | TIME-SCALES VARIABILITY

Here we analyse temporal patterns of the DWT classification and how they are connected to seasonal TC activity. Figure 7a illustrates the DWTs' marginal probabilities during the calibration period, while Figure 7c shows these probabilities per month (three left columns) and for the different yearly seasons (right column). A smooth transition of DWT probabilities over consecutive months and seasons can be observed: starting from austral early spring through austral summer (November–December–January–February) the active DWTs transition from middle to upper lattice; in early austral autumn (March–April) DWTs still concentrate on the upper panel until in May they transition towards the lower panel which is active during the austral winter months (June–July–August–September). Figure 7d aggregates in one plot the calibration period, representing the cumulative proportion of active DWTs along the 365 calendar days (perpetual year) starting from October to September. The colours associated with each DWT facilitate the identification of the typically active mean configurations during the TC season (November–April) which is consistent with the genesis locations in Figure 5 mostly located in the upper half of the lattice (DWTs 1–28). For instance, DWT16 with many genesis events is shown to be active only in January–February (Figure 7d), associated with a continuous band of high index values across the domain, provided by a medium “warm tongue” of surface waters represented by the 29°C isotherm, and MLD values of around 50 m and intense rainfall (Figure 8b) over the north of Vanuatu, Fiji and Samoa. Thus, the seasonality of both predictors plays a significant role and translates to strong variations of TC activity over the year; global observations describe MLD as deep in austral winter (JJA) and shallow in austral summer (DJF) with less than 100 m, and both spring and fall are transitional seasons (Zhang et al., 2018).

Figure 7e displays the DWTs chronology from October to September (x-axis from left to right) for all the seasons from 1982/1983 to 2018/2019 (y-axis from bottom to top). Black dots indicate historical days with active TCs, mostly occurring during the November–April season, with seldom off-season storms in October, May and June. When considering the entire calibration period, some DWTs (2, 9, 10, 16, 21) account for the conditions most prone to TC activity, as the black dots' size over the colourmap represents the relative occurrence

probability of the total number of days with active TCs. This figure helps to identify trends of climate variability at different time scales: the ENSO on interannual time scales, and the Interdecadal Pacific Oscillation (IPO) on decadal time scales. Along the y-axis plot, colour codes next to the TC season indicate the phases of ENSO (Niño/neutral/Niña years, according to the Niño3.4 index) and IPO (positive/negative phases). On one hand, it can be observed a differentiation of predominantly active DWTs in consecutive IPO phases, most persistent during the off-season months (May–October) as well as in transitional months (November–December and March–April). Salinger et al. (2001) also showed that the IPO represents a major source of decadal climate variability in the SWP, which is consistent with the findings of Greenslade and Gregory (2023) who showed that before and after 2000 the relationship between TC activity and several climate indices in the SWP changed significantly. On the other hand, at the interannual time scale, ENSO has been proven to modulate climate variability through the equatorial SST gradient and thus influencing TC activity. The three most intense El Niño seasons (1982/1983, 1997/1998 and 2015/2016) show distinct daily chronologies; seasons 1982/1983 and 1997/1998 remained alternating between DWT 2 and 7 from January till April with a marked zonal warm SST and very intense precipitation north of Vanuatu, Fiji and Samoa; season 15/16 persisted in DWT2, preceded by DWT8 with a warm “tongue” slightly tilted southeast. The rest of El Niño years have common features of combining DWTs 23, 21 and DWTs 9, 10 and 11, all of them with high expected occurrences. El Niño years hold a 25% TC hit rate compared to 11% in La Niña years, while 13% and 9% of the seasons account for each respective phase. Figure 7b shows the histogram of DWT counts with the proportion of Niño/neutral/Niña years (colour bars) and the counts of active TCs (black lines) under each category. DWTs 2, 7, 23, 28 generally occur during El Niño phase (>35% correlation), while La Niña phase correlations are smaller and more distributed (higher than 20% for DWTs 9, 12, 13, 16, 17, 18). It can be noted that these results are consistent with the findings of Magee et al. (2017) who investigated the influence of ENSO and IPO in modulating the spatial characteristics of TC genesis in the SWP; it was confirmed that a strong northeast/southwest spatial modulation of TC genesis was exhibited during El Niño/La Niña phases; whereas the IPO modulates the migration further east/west for the combinations El Niño IPO+/La Niña IPO-. Here the DWT classification corresponding to SST also shows that genesis occurring during El Niño/La Niña phases generally fall under DWTs with a marked northeast/southwest warmer “tongue” of SST (e.g., DWTs

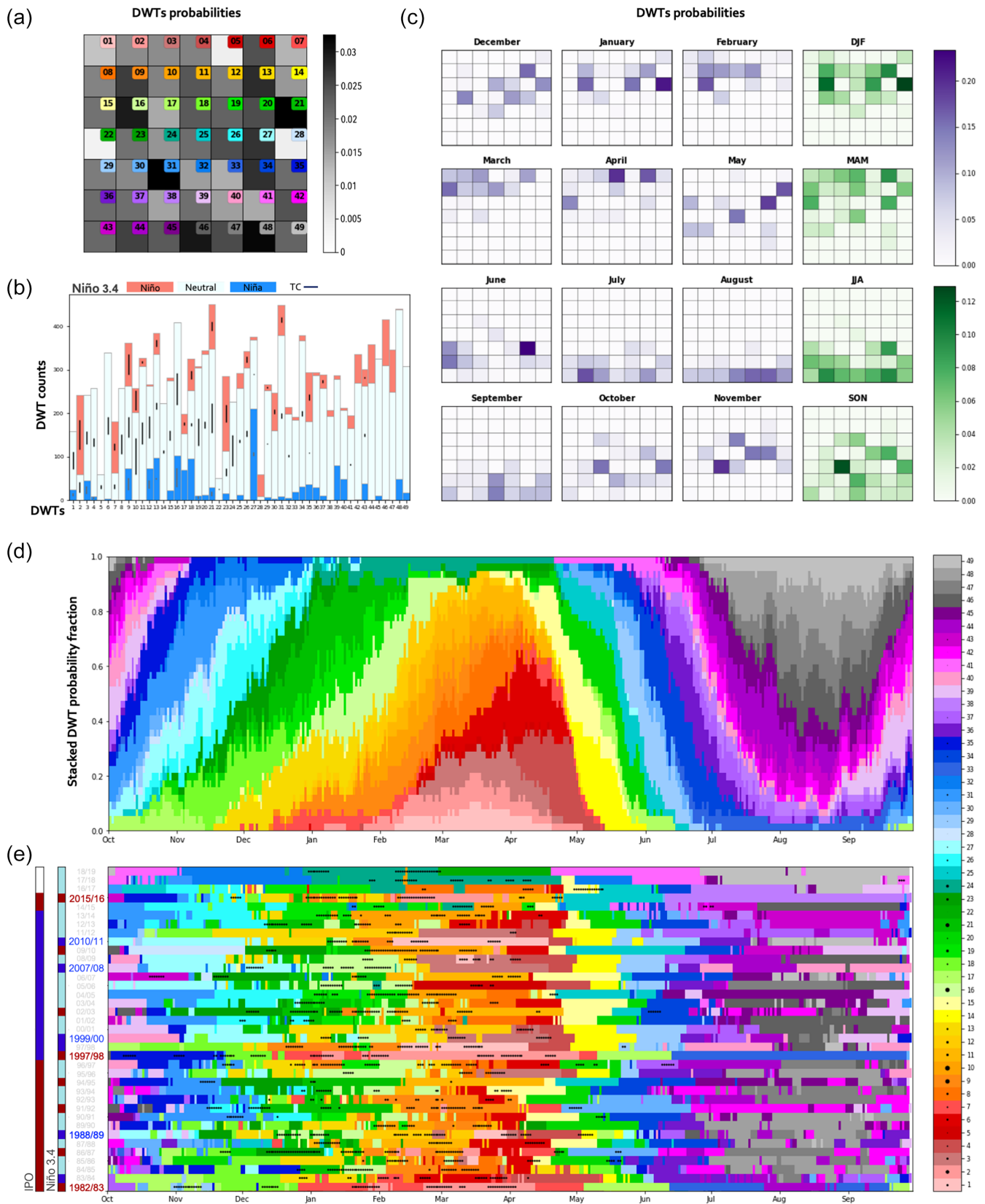


FIGURE 7 Classification of $M = 49$ DWTs: (a) marginal DWTs probabilities; (b) histogram of daily counts per DWT and Niño3.4 index; (c) DWTs probabilities aggregated by months and seasons; (d) stacked DWT probability fraction (y-axis) along the perpetual year from October to September (x-axis); and (e) chronology of DWTs for the calibration period (seasons from 1982/1983 until 2018/2019) with black dots indicating days with active TCs. The right colourmap dot size accounts for TC counts. The left bars indicate the IPO and Niño3.4 phases (positive/neutral/negative) per season [Colour figure can be viewed at wileyonlinelibrary.com]

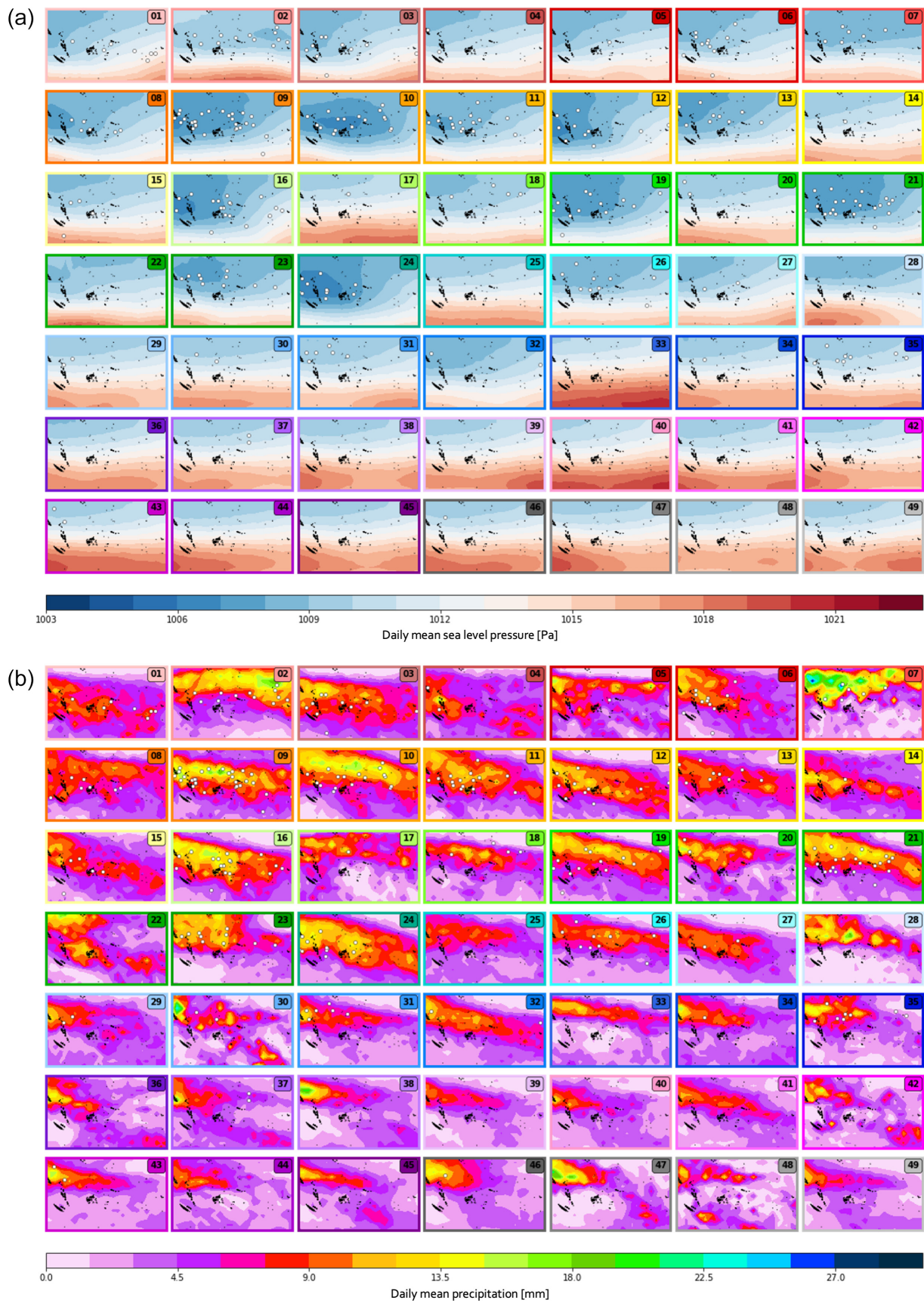


FIGURE 8 Classification of $M = 49$ DWTs for the (a) daily mean precipitation and (b) mean sea level pressure. White dots indicate the location of historical TC genesis [Colour figure can be viewed at wileyonlinelibrary.com]

2, 7, 18, 21, 23, 30, 31 vs. DWTs 1, 3, 6, 9, 12, 16, 19, 27, respectively).

5 | DWT ATMOSPHERIC VARIABILITY

The methodological DWT classification that clusters the defined index predictor into 49 mean synoptic spatial fields over time, allows us to link the associated DWTs with any atmospheric variable. Particularly, here the CFS mean sea level pressure (SLP) fields and the TRMM mean daily spatial precipitation maps were extracted and preprocessed to obtain the mean maps shown in Figure 8a,b, respectively. Both SLP and precipitation are closely connected to TC activity, and their mean synoptic configurations display conditions that are more/less favourable either to trigger genesis events (white dot locations) or to sustain the development of TCs (as informed by the predictand, Figure 6b). On one hand, Figure 8a illustrates the mean synoptic SLP fields, confirming that genesis events are located over low-pressure areas while the highest concentrations happen under SLPs lower than 1009 mbar (i.e., DWTs 9, 10, 11, 12, 16, 19, 21, 23, 24) and where SLP anomalies are pronounced (not shown), generally over Vanuatu, Fiji, Samoa and New Caledonia. The lower half of the lattice includes mean conditions with high-pressure values shifting equatorward and reaching the south of Fiji and the region below 20°S.

On the other hand, Figure 8b shows the lattice of mean patterns from satellite precipitation data, with values ranging up to 12–15 mm daily mean precipitation in most of the upper lattice, and with extreme values of up to 30 mm (DWT 2, 7). The spatial distribution of more intense precipitation denotes the position of the South Pacific Convergence Zone (SPCZ), the most extensive band of convection and precipitation in the Southern Hemisphere, extending from the tropical west Pacific warm pool (west to our domain) towards French Polynesia (Folland et al., 2002; Mirones et al., 2022; Vincent, 1994). Also, this main convection zone modulates the formation and distribution of TCs in the SWP, with genesis and storm trajectories in the region south of the SPCZ (Diamond et al., 2013; Vincent et al., 2011). In fact, genesis locations (white dots) and predictand active cells (Figure 6b) are usually located south to the SPCZ mean position or right below the most intense rainfall band (with mean daily precipitation values higher than 7 mm). In our domain we can observe the diagonally oriented component of the SPCZ in the subtropic (i.e., DWTs 12, 24), which can sometimes tilt towards a zonal orientation (i.e., DWTs 2, 7) resulting in wetter conditions in Tokelau and northern Cook Islands and

drier conditions in Fiji, Tonga, Vanuatu and New Caledonia. The position of the SPCZ varies significantly with ENSO phases, as shown in previous studies (Dowdy et al., 2012; Folland et al., 2002; Vincent et al., 2011; Widlansky et al., 2011). During El Niño conditions warm SST anomalies in eastern and central Pacific decrease trade winds intensity due to weakened zonal SST gradient resulting in the SPCZ expanding to the northeast of its mean position (e.g., DWTs 2, 7, 10, 21). While during La Niña conditions cooler SST (increased zonal gradient) strengthens trade winds which contract the SPCZ southwest of its mean position (Wang et al., 2017) as in DWTs 3, 16, 27. Moreover, although it is present year-round, it can be distinguished in which DWTs the SPCZ is most and least developed during the austral summer (wet) and winter (dry) months respectively, as depicted by the seasonality analysis in section 4.

6 | FORECAST MODEL

To produce the seasonal forecast of TC activity, the ultimate phase of the methodology entails the application of the statistical model over long-term predictions. As presented in section 2, daily predictions of SST and MLD can be downloaded up to 9 months ahead, which allows to generate outlooks of the whole TC season starting from the month of August. These predictor datasets are preprocessed to obtain the associated daily index fields in the domain, which are transformed in the same space of the calibration-fitted PCA to obtain the forecasted daily PCs, and finally to assign each day with the best match centroid of the DWT classification using the minimum distance criteria. This process returns a timeline of DWTs, which are used to retrieve the associated predictand DWT rate maps, and the total expected TC counts is calculated as the summation over time of the predictand values at each $8^\circ \times 8^\circ$ subarea. This proceeding can be applied to the four-times-daily runs available in the CFSv2 operational forecast system, so that the final outlook for the full season is obtained as the mean ensemble. Additionally, it is also possible to aggregate the predictand per months to evaluate seasonal variations of storm frequency.

6.1 | Operational model

The primary goal of this study is to execute an operational forecast system and deliver reliable seasonal outlooks of TC occurrence. For this purpose, the statistical model can be applied to future predictions of global surface temperatures and thermocline depths. Figure 9a shows the seasonal forecast for the upcoming season

2022/2023 from predictions issued on October 1. Here results have been smoothed into $2^\circ \times 2^\circ$ cells spatially, showing more intense activity in the regions of New Caledonia, south of Vanuatu, Samoa and Tonga, although less than 2 TCs are expected in most island territories. Moreover, the season anomaly (Figure 9c) is computed as the difference between the average season from the calibration years (Figure 9b) and the predicted outlook. According to the season anomaly, the October outlook estimates an above-normal activity in the northeastern side of the domain (Solomon Islands, Samoa, Cook Islands) and a below-normal activity in the southwestern side (New Caledonia, south of Vanuatu, Fiji, Tonga). The season outlook can be also produced to estimate the severe TCs season (Figure 9d), including storms of category 3 or higher, which in this case shows one severe TC in the regions of New Caledonia, south of Vanuatu and Tonga. According to the average season of severe TCs (Figure 9e) such predictions indicate near-normal activity in most regions, except above-normal expected activity over Tonga.

6.2 | Reforecast application

Since the operational CFSv2 started operating in April 2011 it is possible to evaluate the model's performance with reforecast data. Figure 10 shows the evolution of full season estimates with predictions issued on the first day of August, September, October and November (first four rows), each output being the ensemble of the four daily runs. It is noticeable how the season outlook changes, mostly intensifying the TC signal in certain regions as the prediction date gets closer to the start of the season. The

last two rows exhibit the mean full season estimates and the differences with observed counts respectively. The mean prediction of those issued on the first days of August–November obtains more accurate results than using the last issue of November (not shown). Usually, the stronger forecasted signal corresponds with the occurrence of a TC, although storm footprints are not always well captured for all the seasons. As an example, season 2015/2016 was an intense El Niño year, which the model underestimated especially in Fiji and Samoa; and the outlook for season 2013/2014 overpredicted (underpredicted) activity in the eastern (western) region by less than 1 TC. Here the maximum error of marginal TC counts ranges from -3.5 to 2.6 , with a slight tendency to overestimate, and RMSE ranges from 0.55 to 3.42 across the targeted 8° cells in the study area (3.42 over Tonga, 1.11 over Fiji, 1.69 over Samoa). Moreover, it is worth comparing with another approach currently producing seasonal outlooks in the study area. The TCO-SP developed by Magee et al. (2020, 2022) generates seasonal outputs for the whole SWP and for 11 island territories using multivariate Poisson regression with indices of multiple climate models, particularly to take into account the spatial diversity of ENSO, with the final outlook for each targeted area being selected as the optimum skilled model from evaluating the whole set of models. They generate forecasts for island territories instead of regular grid cells; nevertheless to provide a qualitative comparison they obtained RMSE values of 2.30 (SWP), 1.17 (Fiji), 1.27 (Tonga).

It should be noted that there are different sources of uncertainty: (1) operational models rely on probabilistic runs of global data, meaning that results highly depend on the quality of the input predictor variables in addition

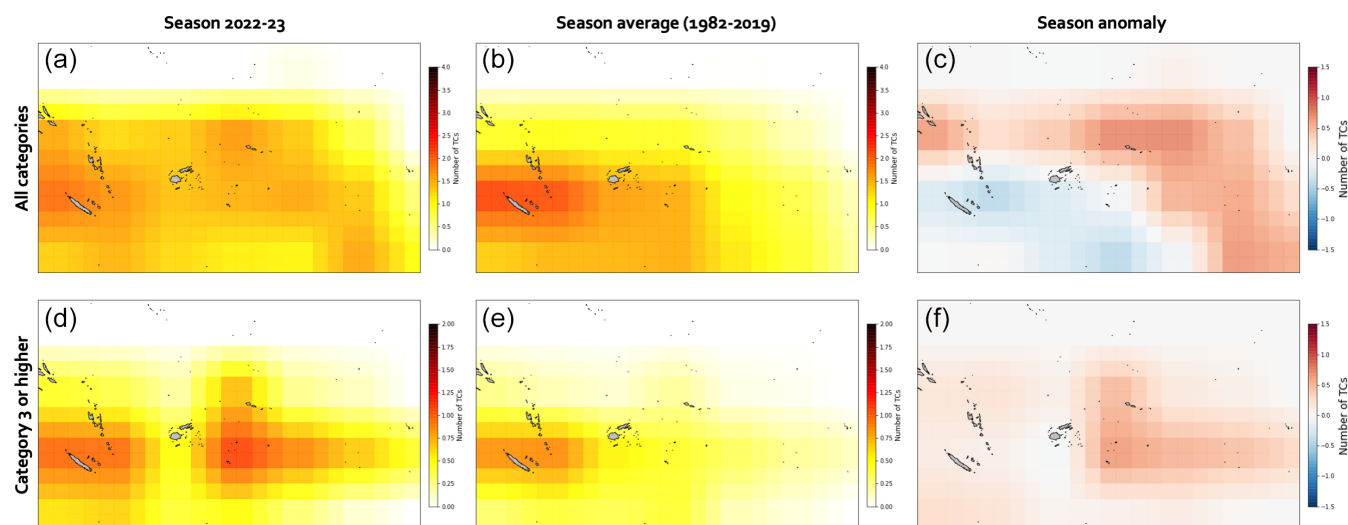


FIGURE 9 Seasonal forecast for the upcoming 2022/2023 season: (a) 4-runs ensemble of the full season and (b) anomaly of the average historical season [Colour figure can be viewed at wileyonlinelibrary.com]

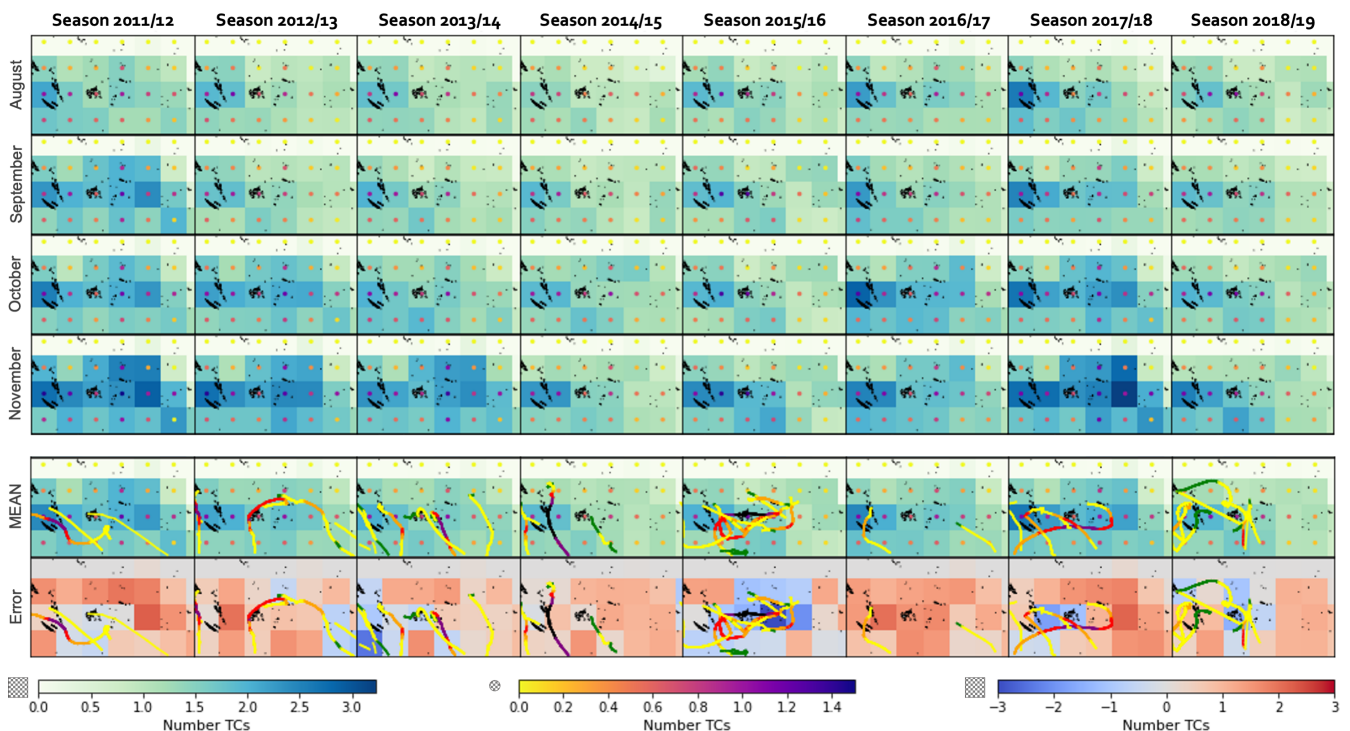


FIGURE 10 Seasonal forecasts from reforecast predictions during seasons 2011/2012 to 2018/2019 (columns) and for dates issued on the first day of months August–November (rows). Last rows for mean outlooks and the error between mean outlook and observed counts [Colour figure can be viewed at wileyonlinelibrary.com]

to the intrinsic model's uncertainty; (2) the proposed statistical model can be calibrated with 40 years of historical data which accounts for past climate variability, although it can be argued that such timeframe may be insufficient to account for large time scale modes of climate variability and to establish more informed relationships predictor–predictand due to the low frequency of the TC events. The methodology is also capable of being implemented over global climate change predictions to evaluate future scenarios of SST and MLD datasets if available.

6.3 | Model validation

Here we explore the skill of the proposed model by implementing the model during the validation seasons (2020/2021, 2021/2022). On one hand, the outcome of the seasonal TC forecast is obtained as shown in Figure 11, with the expected number of TCs aggregated per month (November–April) and for the full season, in shaded colours over subareas of $8^\circ \times 8^\circ$, and with the expected number of TCs of category 3 or higher in the centred coloured dots. Moreover, the error is computed by comparing the model estimate and the observed counts, while coloured lines depict recorded tracks and their category). The off-season months are not included as their contribution is very small. The season

2020/2021 (Figure 11a) was average in number of TCs, with three severe events: TC Yasa (December 11–19) reached category 5 and struck the northern island of Fiji resulting in heavy damage; TC Ana (January 26–February 1, it is shown in both monthly maps as it transitioned in consecutive months) moved south over Fiji as it developed into a category 3; and TC Nirán (March 5–6) was category 5 and hit New Caledonia as it travelled southeast. In this case, the first two tropical cyclones as well as an additional category 1 storm took place in February in DWT 16 (light lime green), which is associated with high probability of TC frequency accompanied by strong rainfall north of Solomon Islands, Vanuatu and Fiji. The conditions during the second half of the season shifted to quite active DWTs 12, 8 and 1 thereby accumulating high rates of occurrence for several weeks. The full season aggregation shows close estimates around two expected TCs in regions of New Caledonia, Vanuatu and south of Fiji, while in Fiji the model underestimated single counts by 1. In comparison, season 2021/2022 (Figure 11b) was less severe in the number of intense TCs and the season forecast overestimated the areas around Fiji. Most tracks were displaced southwest of the domain, which is consistent with the most active DWTs (21, 12, 8) and their associated mean position of the SPCZ bent to the southeast, besides favourable conditions of SST and MLD.

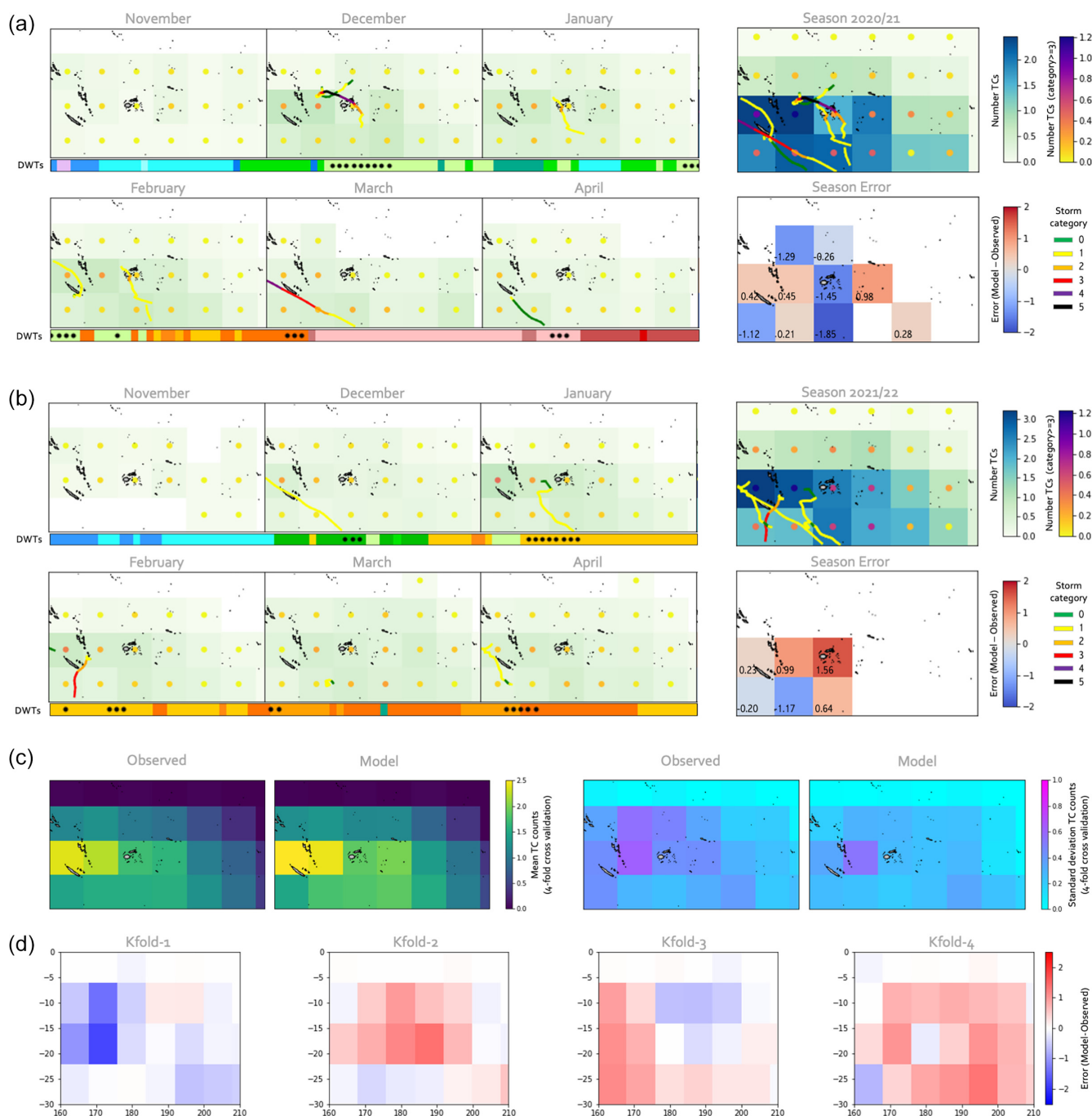


FIGURE 11 Monthly and seasonal forecasts for the validation period of seasons: (a) 2020/2021 and (b) 2021/2022; and cross validation results with (c) mean (left panels) and standard deviation (right panels) of TC counts comparison between historical observations and predicted estimations; and (d) individual k -fold errors between the model and observations [Colour figure can be viewed at wileyonlinelibrary.com]

In addition to the validation of the two most recent seasons, a time series cross validation was performed to quantitatively inform about the skill of the model. For this purpose, the dataset of 40 seasons (from 1982/1983 to 2021/2022) is split into a number of $k = 4$ folds. Iteratively the data sample is split into four groups; thus, 30 years are used to train and calibrate the model whereas the remaining 10 years are used to evaluate the

model's ability to predict when given new data. Therefore, for each iteration it is possible to evaluate the model's distribution of errors compared to the observations for the same period. Figure 11c illustrates, on the left, the resulting mean number of historical observations and the model's expected TC counts, and on the right, their corresponding standard deviation. It can be seen that the expected mean number of TC counts agrees well

with the mean number of observations with a slight overestimation (for instance, the model overestimates by 0.35 in the area of Samoa and Tonga); whereas the standard deviation of the model exhibits slightly lower values compared to observations (with differences up to 0.2 over Fiji, Samoa and Tonga). Figure 11d depicts the absolute error between the model and the observed TC counts for each k -fold iteration; there is spatial variability of over/under estimation with values up to $-1/1$ counts per year, respectively. The sensitivity of results as a function of the cell size can be addressed in the future in order to determine a possible optimum resolution; however, it should be taken into account that potential end users may also be interested in obtaining estimates for different areas of responsibility defined by the island nation territories.

7 | SUMMARY AND DISCUSSION

The proposed methodology is based on finding the statistical relationships between TC activity and spatial configurations of SST and MLD on a daily basis over the SWP Ocean for a period of 38 years. In order to relate SST-MLD nonlinear combinations with TC activity, a tailor-made index predictor [0, 1] was developed in order to derive synoptic configurations using a clustered based method (K -means) at a daily scale in order to retain shorter-term fluctuations compared to only considering phases of long-term modes of climatic indices (El Niño, IPO, among others). Historically, SST has been proven to be one major indicator of TC activity and previous studies also indicated the role of the ocean heat content for both the genesis, growth and trajectories of TCs (Dowdy et al., 2012; Gray, 1979). For example, deeper MLD values can result from intense winds which help mix the surface layer of the ocean and it has been observed that too large depths are not favourable for genesis (Zhang et al., 2018). Additional atmospheric predictors such as wind shear stress, 500-mbar vorticity and humidity, are more complex environmental parameters which have not been included in the present index predictor; however, in the future the method could explore the effect of integrating further predictors if there are available prediction long-term datasets.

The method is conditioned on the available historical record; however, the methodological index predictor contributes to including new potential combinations of SST and MLD. Therefore, it is capable of accounting for future climate change variability configurations. The model compares synoptic patterns with the centroids of the K -means classification thereby assigning statistically obtained daily rates of expected TCs. For this reason, the clustering method is limited and not suited for

extrapolation beyond the known data. Another source of uncertainty deals with errors associated with discrepancies of forecast predictions, although this is partially addressed by performing a probabilistic forecast with an ensemble of prediction runs. Nevertheless, the skill of the model also depends on the quality and realistic spatial distributions of SST and MLD, so different sources of predictions could be used to produce a mean ensemble with reduced uncertainty.

An advantage of the model is the ability to be transferred to other ocean basins. The discretization used here can be tuned to fit different areas and purposes, as the methodology allows for higher resolutions and other unstructured areas of responsibility (i.e., island countries). However, it remains for future research to evaluate the effect of the cell size and its optimum value. In the current layout, results have shown which synoptic types of SST and MLD are favourable to cyclogenesis and activity, with additional information related to concurrent SLP and synoptic precipitation patterns. It is corroborated that the position of SPCZ influences the location of genesis (Diamond et al., 2013), and the displacement of the SPCZ mean position is closely controlled by the ENSO phase (Folland et al., 2002; Vincent et al., 2011; Widlansky et al., 2011). Thus, interannual climate variability plays an important role, as might also be the case with ENSO teleconnections, the IPO and other climatic modes (e.g., the southern annular mode). Diamond and Renwick (2015a) investigated the climatological relationship between TCs in the SWP and the SAM, showing a clear increased frequency of TCs undergoing extratropical transition near New Zealand and the positive phase of SAM; however, they found no clear physical mechanism linking the midlatitude SAM to the genesis of TCs. Nevertheless, in future studies the influence of SAM could be explored to evaluate TC counts especially when evaluating latitudes further away from the Tropics. On the other hand, the Madden-Julian Oscillation (MJO) remains to be the scope of future analysis to potentially improve the proposed model by characterizing its influence over TC counts; Diamond and Renwick (2015b) showed a clear effect of the MJO modulating TC activity and behaviour in the SWP especially in phases 6–7. The chronology of DWTs may also help to gain some understanding and to provide qualitative information on the expected mean configurations.

Since island countries in the SWP are highly exposed as well as vulnerable to severe events, tools to provide valuable estimates of seasonal forecasts some time in advance on top of early warning systems are essential mechanisms to provide governments and stakeholders relevant information to plan ahead mitigation responses to counterbalance negative impacts. Also, seasonal forecasts can transfer useful information to research

institutes to align observational data retrieval with extreme TC events. The proposed model is ready to provide reliable seasonal forecasting outlooks before and during the South Pacific TC season.

AUTHOR CONTRIBUTIONS

Sara O. van Vloten: Writing – original draft; conceptualization; methodology; software; visualization; validation; investigation. **Andrea Pozo:** Writing – review and editing; visualization; software. **Laura Cagigal:** Writing – review and editing; supervision; methodology; funding acquisition. **Fernando J. Méndez:** Writing – review and editing; funding acquisition; supervision; conceptualization; methodology; project administration.

ACKNOWLEDGEMENTS

This work has been partially funded by the Beach4Cast PID2019-107053RB-I00 project, granted by the Spanish Ministry of Science and Innovation. Laura Cagigal acknowledges the funding from the Juan de la Cierva-Formación FJC2021-046933-I/MCIN/AEI/10.13039/501100011033 and the European Union “NextGenerationEU”/PRTR. We would like to give thanks to both anonymous reviewers for their useful comments and suggestions.

ORCID

Sara O. van Vloten  <https://orcid.org/0000-0001-7832-955X>

REFERENCES

- Basher, R.E. & Zheng, X. (1995) Tropical cyclones in the Southwest Pacific: spatial patterns and relationships to Southern Oscillation and sea surface temperature. *Journal of Climate*, 8, 1249–1260. Available from: [https://doi.org/10.1175/1520-0442\(1995\)008<1249:TCITSP>2.0.CO;2](https://doi.org/10.1175/1520-0442(1995)008<1249:TCITSP>2.0.CO;2)
- Camargo, S., Emanuel, K. & Sobel, A. (2007) Use of a genesis potential index to diagnose ENSO effects on tropical cyclone genesis. *Journal of Climate*, 20, 4819–4834. Available from: <https://doi.org/10.1175/JCLI4282.1>
- Chand, S.S. & Walsh, K.J.E. (2009) Tropical cyclone activity in the Fiji region: spatial patterns and relationship to large-scale circulation. *Journal of Climate*, 22, 3877–3893. Available from: <https://doi.org/10.1175/2009JCLI2880.1>
- Diamond, H.J., Lorrey, A.M. & Renwick, J.A. (2013) A Southwest Pacific tropical cyclone climatology and linkages to the El Niño–Southern Oscillation. *Journal of Climate*, 26, 3–25. Available from: <https://doi.org/10.1175/JCLI-D-12-00077.1>
- Diamond, H.J. & Renwick, J.A. (2015a) The climatological relationship between tropical cyclones in the Southwest Pacific and the southern annular mode. *International Journal of Climatology*, 35, 613–623. Available from: <https://doi.org/10.1002/joc.4007>
- Diamond, H.J. & Renwick, J.A. (2015b) The climatological relationship between tropical cyclones in the Southwest Pacific and the Madden–Julian Oscillation. *International Journal of Climatology*, 35, 676–686. Available from: <https://doi.org/10.1002/joc.4012>
- Dowdy, A.J., Qi, L., Jones, D., Ramsay, H., Fawcett, R. & Kuleshov, Y. (2012) Tropical cyclone climatology of the South Pacific Ocean and its relationship to El Niño–Southern Oscillation. *Journal of Climate*, 25, 6108–6122. Available from: <https://doi.org/10.1175/JCLI-D-11-00647.1>
- Emanuel, K. (2003) Tropical cyclones. *Annual Review of Earth and Planetary Sciences*, 31, 75–104. Available from: <https://doi.org/10.1146/annurev.earth.31.100901.141259>
- Espejo, A., Méndez, F.J., Díez, J., Medina, R. & Al-Yayai, S. (2014) Seasonal probabilistic forecast of tropical cyclone activity in the north Indian ocean. *Journal of Flood Risk Management*, 9(4), 379–389. Available from: <https://doi.org/10.1111/jfr3.12197>
- Folland, C.K., Renwick, J.A., Salinger, M.J. & Mullan, A.B. (2002) Relative influences of the Interdecadal Pacific Oscillation and ENSO on the South Pacific Convergence Zone. *Geophysical Research Letters*, 29(13), 21-1–21-4. Available from: <https://doi.org/10.1029/2001GL014201>
- Gergis, J. & Fowler, A.M. (2005) Classification of synchronous oceanic and atmospheric El Niño–Southern Oscillation (ENSO) events for palaeoclimate reconstruction. *International Journal of Climatology*, 25, 1541–1565.
- Gray, W.M. (1979) Hurricanes: their formation, structure and likely role in the tropical circulation. In: Shaw, D.B. (Ed.) *Supplement to meteorology over the tropical oceans*. Bracknell: James Glazier House, pp. 155–218.
- Greenslade, J., & Gregory, P. (2023) - Bureau Research Report - 076, Australian Government, Bureau of Meteorology, <http://www.bom.gov.au/research/publications/researchreports/BRR-076.pdf> [Accessed 29th October 2023].
- Huang, B., Liu, C., Banzon, V.F., Freeman, E., Graham, G., Hankins, B. et al. (2020) *NOAA 0.25-degree daily optimum interpolation sea surface temperature (OISST), version 2.1*. NOAA National Centers for Environmental Information. Available from: <https://doi.org/10.25921/RE9P-PT57>
- Knapp, K., Kruk, M., Levinson, D., Diamond, H. & Neumann, C. (2010) The international best track archive for climate stewardship (IBTrACS): unifying tropical cyclone best track data. *Bulletin of the American Meteorological Society*, 91, 363–376. Available from: <https://doi.org/10.1175/2009BAMS2755.1>
- Knapp, K.R., Diamond, H.J., Kossin, J.P., Kruk, M.C. & Schreck, C.J., III. (2018) *International best track archive for climate stewardship (IBTrACS) project, version 4*. NOAA National Centers for Environmental Information. Available from: <https://doi.org/10.25921/82ty-9e16>
- Magee, A.D., Kiem, A.S. & Lorrey, A.M. (2022) Insights into the usefulness of a new extreme weather guidance tool: the Long-Range Tropical Cyclone Outlook for the Southwest Pacific (TCO-SP). *Bulletin of the American Meteorological Society*, 103, E1120–E1233. Available from: <https://doi.org/10.1175/BAMS-D-21-0108.1>
- Magee, A.D., Lorrey, A.M., Kiem, A.S. & Colyvas, K. (2020) A new Island-scale tropical cyclone outlook for Southwest Pacific nations and territories. *Scientific Reports*, 10, 11286. Available from: <https://doi.org/10.1038/s41598-020-67646-7>
- Magee, A.D., Verdon-Kidd, D.C., Diamond, H.J. & Kiem, A.S. (2017) Influence of ENSO, ENSO Modoki, and the IPO on tropical cyclogenesis: a spatial analysis of the Southwest Pacific

- region. *International Journal of Climatology*, 37, 1118–1137. Available from: <https://doi.org/10.1002/joc.5070>
- Mirones, O., Bedia, J., Fernández-Granja, J.A., Herrera, S., van Vloten, S.O., Pozo, A. et al. (2022) Weather-type-conditioned calibration of Tropical Rainfall Measuring Mission precipitation over the South Pacific Convergence Zone. *International Journal of Climatology*, 43, 1193–1210. Available from: <https://doi.org/10.1002/joc.7905>
- Nicholls, N. (1979) A possible method for predicting seasonal tropical cyclone activity in the Australian region. *Monthly Weather Review*, 107, 1221–1224. Available from: [https://doi.org/10.1175/1520-0493\(1979\)107<1221:APMFPS>2.0.CO;2](https://doi.org/10.1175/1520-0493(1979)107<1221:APMFPS>2.0.CO;2)
- Patricola, C.M., Saravanan, R. & Chang, P. (2016) A teleconnection between Atlantic sea surface temperature and eastern and central North Pacific tropical cyclones. *Geophysical Research Letter*, 44(2), 1167–1174. Available from: <https://doi.org/10.1002/2016GL071965>
- Pielke, R.A. & Landsea, C.N. (1999) La Niña, El Niño, and Atlantic Hurricane damages in the United States. *Bulletin of the American Meteorological Society*, 80(10), 2027–2033. Available from: [https://doi.org/10.1175/1520-0477\(1999\)080<2027:LNAENO>2.0.CO;2](https://doi.org/10.1175/1520-0477(1999)080<2027:LNAENO>2.0.CO;2)
- Pillay, M.T. & Fitchett, J.M. (2021) On the conditions of formation of Southern Hemisphere tropical cyclones. *Weather and Climate Extremes*, 34, 100376. Available from: <https://doi.org/10.1016/j.wace.2021.100376>
- Refugees International. (2022) Tropical Cyclone Yasa: Fiji's second category 5 cyclone in a year. Available from <https://www.refugeesinternational.org/reports/2021/3/15/tropical-cyclone-yasa-fijis-second-category-5-cyclone-in-a-year#:~:text=TC%20Yasa%20wiped%20out%20entire,infrastructure%2C%20livelihoods%2C%20and%20agriculture> [Accessed 3 November 2022]
- Saha, S., Moorthi, S., Pan, H., Wu, X. & Wang, J. (2010) The NCEP Climate Forecast System Reanalysis. *Bulletin of the American Meteorological Society*, 91, 1015–1057. Available from: <https://doi.org/10.1175/2010BAMS3001.1>
- Saha, S., Moorthi, S., Wu, X. & Wang, J. (2014) The NCEP Climate Forecast System Version 2. *Journal of Climate*, 27, 2185–2208. Available from: <https://doi.org/10.1175/JCLI-D-12-00823.1>
- Salinger, J., Renwick, J.A. & Mullan, A.B. (2001) Interdecadal Pacific Oscillation and South Pacific climate. *International Journal of Climatology*, 21(14), 1705–1721. Available from: <https://doi.org/10.1002/joc.691>
- Smith, R.K. (2006) *Lectures on tropical cyclones*. Lectures on tropical cyclones. https://www.meteo.physik.uni-muenchen.de/.../Lectures/Tropical_Cyclones/060510_tropical_cyclones-1.pdf
- Tropical Rainfall Measuring Mission. (2011) *TRMM (TMPA) Rainfall Estimate L3 3 hour 0.25 degree × 0.25 degree V7*. Greenbelt, MD: Goddard Earth Sciences Data and Information Services Center (GES DISC). Available from: <https://doi.org/10.5067/TRMM/TMPA/3H/7>
- Vincent, D.G. (1994) The South Pacific Convergence Zone (SPCZ): a review. *Monthly Weather Review*, 122(9), 1949–1970. Available from: [https://doi.org/10.1175/1520-0493\(1994\)122,1949:TSPCZA.2.0.CO;2](https://doi.org/10.1175/1520-0493(1994)122,1949:TSPCZA.2.0.CO;2)
- Vincent, E.M., Lengaigne, M., Menkes, C.E., Jourdain, N., Marchesiello, C.P. & Madec, G. (2011) Interannual variability of the South Pacific Convergence Zone and implications for tropical cyclone genesis. *Climate Dynamics*, 36, 1881–1896. Available from: <https://doi.org/10.1007/s00382-009-0716-3>
- Vissa, N.K., Satyanarayana, A.N.V. & Prasad, K.B. (2012) Response of upper ocean during passage of MALA cyclone utilizing ARGO data. *International Journal of Applied Earth Observation and Geoinformation*, 14, 149–159. Available from: <https://doi.org/10.1016/j.jag.2011.08.015>
- Wang, C., Deser, C., Yu, J.-Y., DiNezio, P. & Clement, A. (2017) El Niño and Southern Oscillation (ENSO): a review. In: Glynn, P.-W., Manzello, D. & Enochs, I.C. (Eds.) *Coral reefs of the eastern tropical Pacific: persistence and loss in a dynamic environment*. Dordrecht, Netherlands: Springer Netherlands, pp. 85–106.
- Widlansky, M.J., Webster, P.J. & Hoyos, C.D. (2011) On the location and orientation of the South Pacific Convergence Zone. *Climate Dynamics*, 36, 561–578. Available from: <https://doi.org/10.1007/s00382-010-0871-6>
- Zhang, Y., Xu, H., Qiao, F. & Dong, C. (2018) Seasonal variation of the global mixed layer depth: comparison between Argo data and FIO-ESM. *Frontiers in Earth Science*, 12, 24–36. Available from: <https://doi.org/10.1007/s11707-017-0631-6>

How to cite this article: van Vloten, S. O., Pozo, A., Cagigal, L., & Méndez, F. J. (2023). Seasonal forecast of tropical cyclones in the Southwest Pacific Ocean. *International Journal of Climatology*, 43(16), 7851–7869. <https://doi.org/10.1002/joc.8295>